






Simultaneous measurements of nuclear-spin heat capacity, temperature, and relaxation in GaAs microstructures

M. Vladimirova , S. Cronenberger, A. Colombier , and D. Scalbert 
Laboratoire Charles Coulomb, CNRS, Université de Montpellier, Montpellier, France

V. M. Litvyak  and K. V. Kavokin 
Spin Optics Laboratory, St. Petersburg State University, Ulyanovskaya 1, St. Petersburg 198504, Russia

A. Lemaître 
Université Paris-Saclay, CNRS, Centre de Nanosciences et de Nanotechnologies, 91120 Palaiseau, France

 (Received 8 December 2021; revised 15 February 2022; accepted 8 March 2022; published 11 April 2022; corrected 2 June 2022)

Heat capacity of the nuclear-spin system (NSS) in GaAs-based microstructures has been shown to be much greater than expected from dipolar coupling between nuclei, thus limiting the efficiency of NSS cooling by adiabatic demagnetization. It was suggested that quadrupole interaction induced by some small residual strain could provide this additional reservoir for the heat storage. We check and validate this hypothesis by combining nuclear-spin relaxation measurements with adiabatic remagnetization and nuclear magnetic resonance experiments, using electron spin-noise spectroscopy as a unique tool for detection of nuclear magnetization. Our results confirm and quantify the role of the quadrupole splitting in the heat storage within NSS and provide additional insight into the fundamental, but still actively debated relation between a mechanical strain and the resulting electric field gradients in GaAs.

DOI: [10.1103/PhysRevB.105.155305](https://doi.org/10.1103/PhysRevB.105.155305)

I. INTRODUCTION

In n -doped semiconductors donor-bound electron spins and the lattice nuclei spin system (NSS) are coupled via hyperfine interaction [1]. Their magnetic moments and interaction energies, as well as their coupling to light, to crystal lattice vibrations, and to electric and magnetic fields, differ dramatically. The resulting physics, which is best studied in n -GaAs, is quite complex. However, if sufficient NSS stability is reached, it may potentially offer novel applications for quantum information technologies [2–10].

In this context, precise knowledge and control of nuclear quadrupole effects in n -GaAs and GaAs-based heterostructures have attracted substantial attention. Indeed, in semiconductors with cubic symmetry containing isotopes with spin $I > 1/2$, quadrupole interaction induced by strain splits NSS energy states [cf. Fig. 1(a)] and thus strongly affects NSS thermodynamics [11–14]. The effects of strain are particularly important in heterostructures, such as quantum wells [15] and quantum dots (QDs), and were extensively studied in both single QDs [4,16] and QD ensembles [17]. More recently, quadrupole effects in bulk n -GaAs have been evidenced, suggesting the importance of the precise control of both strain and electric field when NSS needs to be efficiently cooled down [18]. Moreover, the parameters of different isotopes determining the relation between the strain tensor elements and the resulting gradients of the electric fields remain controversial [16,18–20]. This is partly due to the lack of nondestructive and

nonperturbative experimental techniques, capable of probing nuclear magnetic resonances (NMR) at low and zero magnetic field, where quadrupole splittings between spin levels dominate over Zeeman ones.

Indeed, traditional optically detected NMR experiments addressing QD ensembles are limited to the field range given by the Hanle curve, and suffer from huge broadening due to inhomogeneity of the electric field gradient experienced by the nuclei [17]. On the other hand, since the pioneering experiments of Gammon *et al.* resolving the photoluminescence fine structure in individual QDs [21], remarkable progress has been achieved in the NSS control in such structures [4]. However, in order to reach measurable splitting, a relatively high magnetic field, where the Zeeman effect dominates over the quadrupole one, should be applied.

Spin noise spectroscopy (SNS) could be promising for this purpose. It has been shown that electron spin noise can nondestructively relay properties of the nuclear environment through the statistics of electron spin interaction with the total nuclear polarization [22–26]. SNS is based on the nonperturbative detection of the spin polarization noise via fluctuations of the Kerr or Faraday rotation of the off-resonant probe beam polarization; see Fig. 1(b) [27,28].

It is important to stress that although we aim to probe the NSS, rather than electron spin, what is measured in practice is the electron spin-noise spectrum in the megahertz frequency range. This approach differs from the one adopted by Berski *et al.* [24], who directly measured, in n -GaAs, nuclear-spin

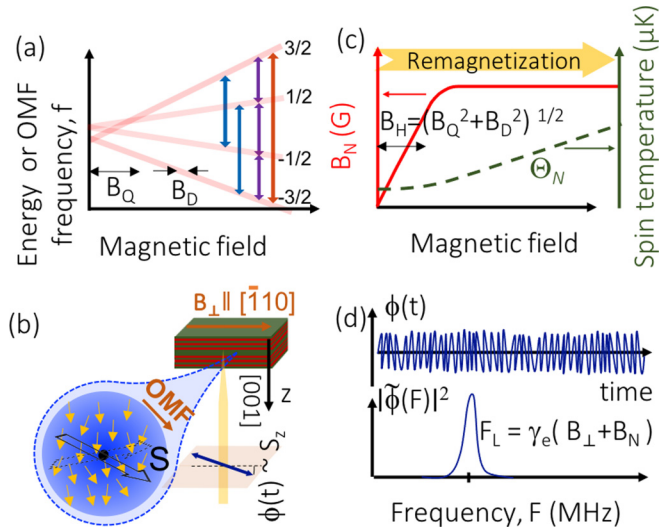


FIG. 1. (a) Schematic representation of quadrupole-split nuclear-spin levels. Arrows indicate NMR transitions. (b) Sketch of the donor-bound electron spin interacting with the underlying nuclear spins. (c) Overhauser field B_N and the corresponding nuclear-spin temperature Θ_N as functions of the magnetic field according to spin temperature theory. B_H is a field that characterizes NSS heat capacity. (d) Fluctuations of the electron spin detected via Kerr rotation in time domain within 0.5 GHz frequency band and the corresponding Fourier power spectrum.

noise associated with different isotopes in the kilohertz frequency range. Such direct nuclear-spin measurements are quite difficult since NSS does not couple directly with light, but they are particularly useful to address the nuclear-spin dynamics at low magnetic fields where it is hardly accessible otherwise.

In electron SNS, the fluctuation spectrum exhibits a pronounced peak at the Larmor frequency corresponding to the total magnetic field experienced by electrons. It is given by the sum of the external field B_{\perp} and Overhauser field B_N , an effective nuclear field resulting from the hyperfine interaction; see Fig. 1(d). Therefore, any variation of the NSS polarization, either due to relaxation or when the external magnetic field is reduced, results in a change of the Larmor frequency and thus in a shift of the electron spin-noise peak. This shift is proportional to the Overhauser field, but is not isotope selective. We have demonstrated that the evolution of nuclear-spin polarization during optical pumping, relaxation, and remagnetization through the zero field can be monitored via this shift with subsecond resolution [23,25,29,30].

These experiments, performed on *n*-GaAs layers, revealed that the relaxation rates of optically cooled NSS under magnetic fields below 10 G are dramatically enhanced. We also measured the huge heat capacity characterized by the so-called local field, also of the order of ≈ 10 G. This value is much higher than expected from magnetic dipole-dipole interaction $B_D \approx 1.5$ G [31]. This result is illustrated in Fig. 1(b). It shows how the Overhauser field (solid line) and the nuclear-spin temperature (dashed line) in a cold NSS vary during remagnetization from zero to high magnetic field. The dependence of the Overhauser field on the magnetic field B is related

to the nuclear-spin temperature Θ_N [1],

$$B_N = \frac{hBb_N I(I+1)\bar{\gamma}_N}{3k_B\Theta_N}. \quad (1)$$

Here, $\bar{\gamma}_N = \sum_i A_i \gamma_{Ni}$ is the average gyromagnetic ratio, A_i (γ_{Ni}) is the abundance (gyromagnetic ratio) of the *i*th isotope (see Table I), h and k_B are the Planck and Boltzmann constants, respectively, and b_N is the Overhauser field at saturation of the nuclear magnetization, in GaAs, $b_N = 5.3$ T. The magnetic field below which Θ_N remains constant reveals the heat capacity of the NSS. In the following, it will be referred to as the heat capacity field, B_H [32]. The value $B_H \gg B_D$, as shown in Fig. 1(c), is a fingerprint of the enhanced NSS heat capacity as compared to the traditional spin temperature theory [1,30,33].

Because in GaAs the spin of all isotopes $I = 3/2$, it was suggested that such an enhanced NSS heat capacity could be explained by the quadrupole splitting of nuclear-spin energy levels induced by some small residual strain; see Fig. 1(b). The corresponding effective field B_Q is the one where Zeeman and quadrupole energies become comparable. In the remagnetization experiment illustrated in Fig. 1(a), one would expect

$$B_H = \sqrt{B_D^2 + B_Q^2}. \quad (2)$$

However, in the absence of NMR experiments that could provide direct access to quadrupole energies, these ideas remain unconfirmed.

In this work, we design and implement a different technique, where NMR is detected by electron SNS. This technique allows us to ascertain the effects of the quadrupole interaction on nuclear spin dynamics. NSS absorption spectra in the radio-frequency (rf) range are measured as a function of magnetic field from zero to 100 G. In order to reach the detection sensitivity required for such experiments (subsecond integration times), we use an *n*-GaAs layer embedded in a microcavity [34] and adopt the homodyne detection scheme for the spin-noise measurements [35–37]. The analysis of the NMR spectra allows us (i) to evaluate quantitatively quadrupole energies and confirm the impact of the quadrupole interaction on the heat capacity of the NSS. The quadrupole energies extracted from the NMR spectra appear to be consistent with the heat capacity fields measured in the NSS remagnetization experiments and with the spin temperature theory; (ii) to provide additional insight into relative values of the so-called gradient-elastic tensor S_{ijkl} for Ga and As isotopes. This fundamental parameter determines the relation between the strain tensor ϵ_{kl} and the resulting electric field gradients at each atomic site $V_{ij} = \sum_{k,l} S_{ijkl} \epsilon_{kl}$. Its values are isotope dependent and are still actively debated in the literature [16,18–20].

II. SAMPLE

We study the microcavity sample cut out from the same wafer as in Ref. [30]: a Si-doped $3\lambda/2$ GaAs layer (cavity mode at ≈ 830 nm in the studied piece of the sample) with donor concentration $n_D \approx 2 \times 10^{15}$ cm⁻³ sandwiched between two Bragg mirrors, in order to enhance the sensitivity of the SNS (quality factor $\approx 2 \times 10^4$). The front (back)

TABLE I. Quadrupole parameters obtained in this work and those taken from the literature, as well as other GaAs parameters used in the calculations: stiffness tensor elements, isotope abundancies, quadrupole moments, and gyromagnetic ratios.

	^{69}Ga	^{71}Ga	^{75}As	$^{75}\text{As}/\text{Ga}$
Q (10^{-30} m 2) [44]	10.7	17.1	31.4	
Abundance	0.3	0.2	0.5	
γ_N (kHz/G) [44]	0.82	0.64	0.45	
C_{11} (10^{-10} N/m 2) [45]	12	12	12	
C_{12} (10^{-10} N/m 2) [45]	5.4	5.4	5.4	
C_{44} (10^{-10} N/m 2) [45]	6.2	6.2	6.2	
E_{QZ}/h (kHz)	$-10. \pm 0.5$	$-6. \pm 0.5$	20 ± 0.5	
E_{\perp}/h (kHz)	-3.5 ± 0.5	-2.2 ± 0.5	12.5 ± 0.5	
ζ (degrees with [100] axis)	-68 ± 5	-68 ± 5	-33 ± 5	
S_{11} (10^{21} V/m 2)	-31.7 [19], -22 [16]	-31.7 [19], -22 [16]	34 [19], 24.2 [16]	-1.07 [19], -1.1 [16,18]
S_{11} (^{75}As)/ S_{11} (Ga) [this work]				-1.1 ± 0.1
S_{44} (10^{21} V/m 2)	32 [19], 9 [20]	32 [19], 9 [20]	68 [19], 48 [20]	2.1 [19], 5.3 [20], 1.9 [18]
S_{44} (^{75}As)/ S_{44} (/ , Ga) [this work]				2.5 ± 0.4

mirrors are distributed Bragg reflectors composed of 25 (30) pairs of AlAs/Al $_{0.1}$ Ga $_{0.9}$ As layers. The sample is grown on a 400- μm -thick [001]-oriented GaAs substrate and placed in a cold finger cryostat at $T = 6$ K. A 30-spikes copper coil is placed on top of the sample to create an oscillating magnetic field (OMF). It is directed at 45° out of the sample plane [38].

III. NMR AND REMAGNETIZATION DETECTED BY THE ELECTRON SPIN NOISE

The principles of NMR and NSS remagnetization detected by electron spin noise are sketched in Fig. 2. Prior to the measurement, any preexisting polarization in the NSS is erased by the OMF $B_{RF} = 0.3$ G during 20 s, its frequency sweeping between 0 and 50 kHz (stage 1). At stage 2, the NSS is polarized by optical pumping in the presence of a longitudinal magnetic field $B_z = 150$ G during typically 30 s (circularly polarized laser emitting at 770 nm). This is followed by 30 s of dark time under the same magnetic field to allow for fast relaxation of the nuclear spins under the donors orbits while keeping the bulk nuclei polarized (stage 3). After that, the NSS is adiabatically demagnetized down to zero magnetic field (stage 4). This last stage is important to include in the protocol, despite some additional NSS warm-up that it causes. Indeed, it ensures NSS thermalization and a transfer of the optically pumped energy stored in the Zeeman reservoir to-

wards internal degrees of freedoms, which is the dipole-dipole reservoir. This additional nuclear-spin relaxation during stage 4 does not play any role in the experiment, provided that the NSS is strongly polarized (which is the case). What matters is to start the detection of the NSS demagnetization or absorption each time at the same spin temperature.

The four stages of preparation of the NSS are identical for both NMR and remagnetization experiments; see Fig. 2(a).

The remagnetization experiments are similar to those reported in Ref. [30]. After preparation (stages 1–4), a set of electron spin-noise spectra under the in-plane magnetic field that increases from $B = 0$ to $B = 100$ G is measured every 2 G; see Fig. 2(b). The measured frequency F_L of the electron spin-noise spectral peak at a given field B_{\perp} is directly related to the Overhauser field B_N ,

$$F_L = F_B + F_N = \gamma_e(B_{\perp} + B_N), \quad (3)$$

where $\gamma_e = 0.62$ MHz/G is the electron gyromagnetic ratio in GaAs. Representative spectra measured at several values of the magnetic field are shown in Fig. 3.

Measurement of each point of the NMR spectrum at a given field B (either B_{\perp} or B_z) corresponding to a given rf frequency f consists in three steps, illustrated in Fig. 2(c): detection of the electron spin noise and its peak frequency F_L in the sample under magnetic field $B_{\perp} = 100$ G in order to

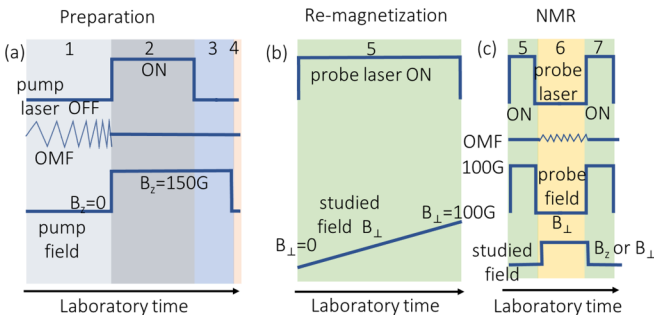


FIG. 2. Time sequence used for (a) NSS preparation, (b) remagnetization, and (c) NMR experiments.

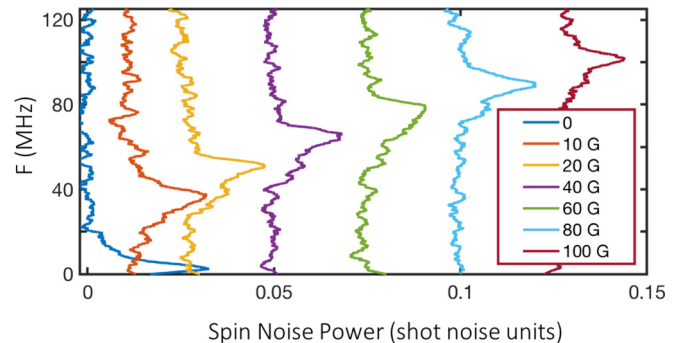


FIG. 3. SN spectra measured at different values of the magnetic field during adiabatic remagnetization.

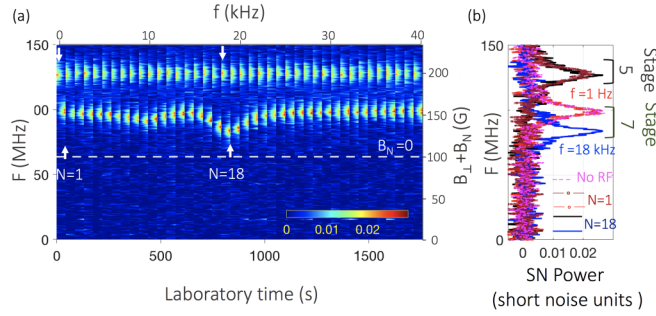


FIG. 4. (a) 40 pairs of color-coded SN spectra required for NSS absorption measurement at $B = 0$. Each pair is recorded within steps 5 and 7 of the NMR experiment that includes both preparation and detection. The measurements are realized in a single run, one after another, for different OMF frequencies f . The bottom scale indicates the laboratory time, and the top scale is the corresponding OMF frequency. Such set of measurements allows us to reconstruct the NMR spectrum at $B = 0$. Intensities are given in the units of spin to shot noise ratio. (b) Pairs $N = 1$ ($f = 1$ Hz) and $N = 18$ ($f = 18$ kHz) of the spin-noise spectra shown in (a). At $f = 1$ Hz, NSS absorbs energy very weakly, so that the corresponding stage 7 spectrum is identical to the one measured in the absence of the OMF (dashed magenta line) and its peak position is essentially governed by NSS relaxation. The peak of the spectrum corresponding to $N = 18$ is shifted to much lower frequency; this shift is governed by NSS absorption.

evaluate the Overhauser field prior to absorption (stage 5), application during 3 s of the OMF at a given frequency f in the rf range and at a given magnetic field B at which the rf absorption is studied (stage 6), and again detection of the electron spin noise and its frequency F_L under magnetic field $B_{\perp} = 100$ G (stage 7). This allows us to deduce from Eq. (3) to which extent the Overhauser field has decreased during stage 6.

Typical spin-noise spectra measured at stages 5 and 7 are shown in Fig. 4(b). The corresponding field under study is $B = 0$. The OMF frequencies applied during stage 6 are $f = 1$ Hz where NSS absorbs energy very weakly, and $f = 18$ kHz where NSS absorption is strong. The spectrum measured during stage 7 in the absence of OMF is shown by the dashed magenta line for comparison. The shift between the electron spin-noise spectral peaks measured during stages 5 and 7 contains two contributions. The first is rf independent and is due to some weak, but unavoidable NSS relaxation during measurement. It can be evaluated by performing identical measurements in the absence of the OMF during stage 6; see the dashed magenta line in Fig. 4(b). The second contribution is proportional to the NSS absorption at a given OMF frequency f . It is negligibly small at $f = 1$ Hz, but when f matches the energy difference between spin states of one of the isotopes (as for $f = 18$ kHz, where f matches ^{75}As resonance), the radiation is efficiently absorbed and the spectrum shifts more than in the absence of the OMF field.

The entire absorption spectrum (or NMR spectrum) can be constructed by repeating the protocol (stages 1–7) at different values of f . The details of this procedure are given in Appendix A 1. An example of the raw data obtained in an NMR experiment addressing NSS absorption at $B = 0$ is shown in

Fig. 4(a). A color-coded set of 40 pairs of electron spin-noise spectra measured in units of the ratio between spin and shot noise is shown as a function of laboratory time (bottom scale). The corresponding OMF frequency f is indicated on the top. For each value of f , two spectra are systematically measured: one before application of the OMF (in this case, the electron spin-noise peak frequency F_L does not depend on the OMF frequency f) and one after. The left scale shows spin-noise frequency and the right scale shows the corresponding total magnetic field experienced by the electrons, $B_{\perp} + B_N = F/\gamma_e$, where $B_{\perp} = 100$ G. One can see that B_N is significantly smaller after application of the OMF at $f \approx 8$ kHz and at $f \approx 20$ kHz. These frequencies characterize nuclear-spin splittings at $B = 0$; cf. Fig. 1(a). We anticipate that the higher frequency is related to quadrupole-split states of ^{75}As which have the highest quadrupole moment, and the lower one to closely lying transitions of ^{71}Ga and ^{69}Ga isotopes.

It is important to note that in most of SNS experiments, the magnetic field is modulated to eliminate spin-independent signals [39]. Such approach is not suitable for studies of the NSS because nuclear spins get depolarized by nonadiabatically varying magnetic fields. To avoid this effect and also to increase the sensitivity, in this work we use a homodyne detection scheme [35]. This allows us to use the probe power as low as $150 \mu\text{W}$ focused on a $30\text{-}\mu\text{m}$ -diameter spot. We detect the spectra in two mutually orthogonal linear polarizations, that is, either parallel (which contains useful information about electron spin noise) or orthogonal to the local oscillator polarization. The spin-noise spectrum is obtained by taking the difference between these spectra, in order to get rid of the background noise.

IV. NMR SPECTRA AND THEIR INTERPRETATION

A set of color-coded NMR spectra measured under in-plane static magnetic field $B_{\perp} \parallel [110]$ and at $B_z \parallel [001]$ is shown in Figs. 5(a) and 5(b). In order to understand these spectra in terms of the OMF-induced transitions between spin states of the three GaAs isotopes, we must calculate the energy spectrum of the NSS. It is determined by both the quadrupole interaction and the Zeeman effect: $\hat{H}^i = \hat{H}_Q^i + \hat{H}_Z^i$, where \hat{H}_Q^i (\hat{H}_Z^i) describes quadrupole (Zeeman) interaction [40]. The energy levels of each isotope are given by the eigenvalues of the Hamiltonian \hat{H}^i , and the NMR transition frequencies are given by their differences $f_{kl}^i = (E_k^i - E_l^i)/h$. The OMF induces spin transitions between a pair of states k and l of the i th isotope if the OMF frequency matches the energy difference between their energy levels E_k and E_l . The probability of the corresponding transition is given by $P_{kl}^i \propto M_{kl,i}^2$, where $M_{kl} = \langle \Psi_k | H_{OMF} | \Psi_l \rangle$ is the matrix element of the Hamiltonian describing the Zeeman interaction of the nuclear spins with the OMF.

The quadrupole Hamiltonian of the i th isotope in the presence of the in-plane biaxial strain can be written as [11]

$$\hat{H}_Q^i = \frac{E_{QZ}^i}{2} \left[\hat{I}_z^2 - \frac{I(I+1)}{3} \right] + \frac{E_{QR}^i}{2\sqrt{3}} [(\hat{I}_x^2 - \hat{I}_y^2)] + \frac{E_{QI}^i}{2\sqrt{3}} [(\hat{I}_x \hat{I}_y + \hat{I}_y \hat{I}_x)], \quad (4)$$

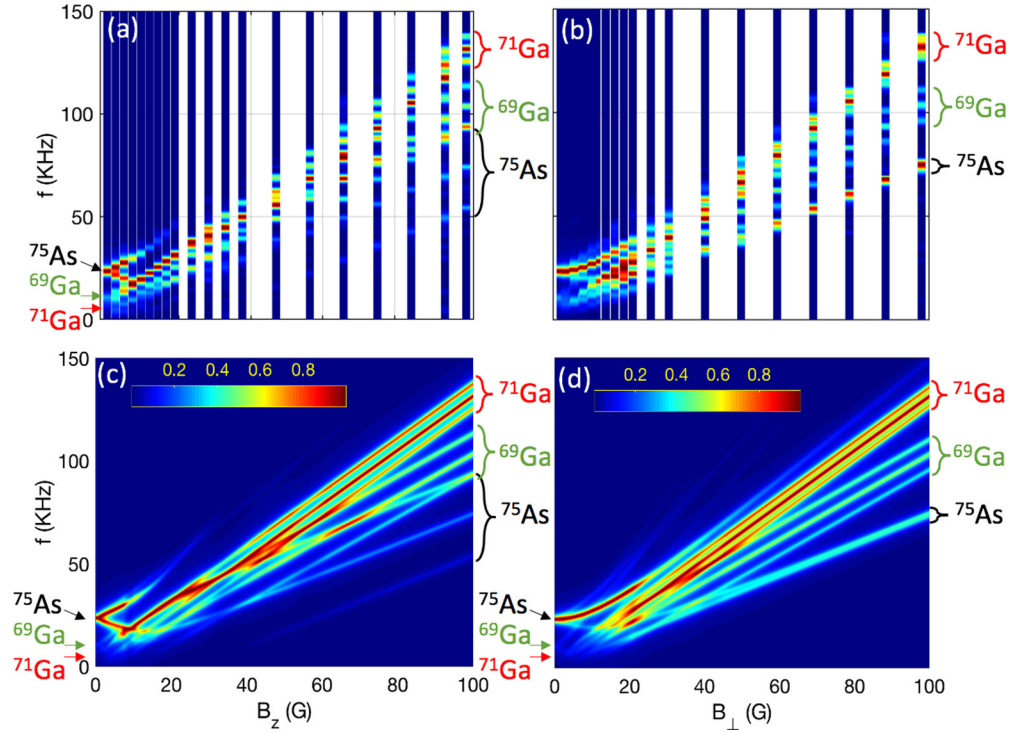


FIG. 5. Color-coded NSS absorption spectra (a),(b) measured and (c),(d) calculated at different values of magnetic field parallel to either the (b) $[\bar{1}10]$ or (a) $[001]$ crystallographic axis. All the spectra are normalized to unity.

where $E_{QR}^i = E_{Q\perp}^i \cos 2\zeta^i$ and $E_{QI}^i = E_{Q\perp}^i \sin 2\zeta^i$. It is determined by three parameters: E_{QZ}^i —the quadrupole energy along the growth axis, $E_{Q\perp}^i$ —the in-plane quadrupole energy, and ζ^i —the angle between the principal axis of the electric field gradient tensor V_{ij} and the $[100]$ crystal axis.

The ensemble of the absorption spectra shown in Figs. 5(a) and 5(b) can be understood by fitting this simple model to the observed transition frequencies. This yields three parameters per isotope. They are summarized in Table I together with other relevant parameters (abundances, quadrupole moments, and gyromagnetic ratios) taken from the literature. Assuming that all transitions have a Lorentzian shape broadened by dipole-dipole interaction ($\Delta f_D = 1.5$ kHz), we calculate the resulting absorption spectra at different values and two orientations of the magnetic field, as shown in Figs. 5(c) and 5(d).

One can see that most of the salient features of the measured spectra are faithfully reproduced. Indeed, for $B = 0$, the measured and calculated spectra are presented separately in Fig. 6(a), where the ^{75}As absorption (higher-frequency line) dominates the spectrum. At small fields parallel to the growth axis B_z , the ^{75}As absorption line splits into two lines, which shift linearly with B_z . By contrast, under in-plane field B_\perp , the ^{75}As absorption line shifts quadratically.

At strong field $B = 100$ G, we identify for each isotope a triplet of lines, including a central line and a pair of satellites. Measured and calculated spectra at $B = 100$ G oriented either along the $[\bar{1}10]$ or $[001]$ crystallographic axis are shown in Figs. 6(b) and 6(c), respectively. The strongest absorption is observed for ^{71}Ga . In the presence of the longitudinal field

B_z , the splitting between the central line and its satellites is the smallest for ^{71}Ga and the highest for ^{75}As . By contrast, under an in-plane field B_\perp , this splitting vanishes for ^{75}As . This latter fact results from the sign difference in the in- (E_{QI}) and out-of-plane (E_{QZ}) quadrupole parameters for Ga and As. We will show below that this implies a particular sign relation between different elements of the gradient-elastic tensor elements S_{11} , S_{44} for Ga and As.

Two more observations could be drawn from the comparison between the model and the measured spectra. First, the generic Lorentzian broadening $\Delta f_D = 1.5$ kHz common

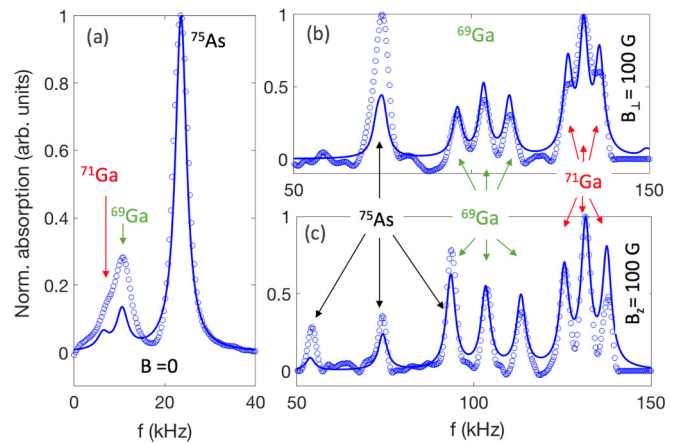


FIG. 6. NSS absorption spectra measured (symbols) and calculated (lines) at (a) $B = 0$, (b) $B_z = 100$ G, which is parallel to the $[001]$ crystal axis, and (c) $B_\perp = 100$ G, which is parallel to $[\bar{1}10]$. All the spectra are normalized to unity.

for all transitions fits the data satisfactorily. The fact that this linewidth is identical for all transitions and comparable with the one expected from dipole-dipole broadening [see, also, Fig. 1(a)] suggests that NSS is efficiently thermalized at $B \approx B_D$. Second, the relative intensities of Ga and As absorption are not faithfully reproduced by the model: at low magnetic field, it underestimates Ga absorption as compared to As, and at high field, the situation is inverted. We have no solid physical explanation for this discrepancy, which was also reported in Ref. [24], but not in Ref. [18]. Nevertheless, it could simply result from an ill-defined direction of the OMF field.

V. REMAGNETIZATION OF THE NSS IN THE PRESENCE OF THE QUADRUPOLE EFFECTS

The above measurements show that quadrupole interaction is much stronger in this sample than dipole-dipole interaction. In this section, we compare quantitatively the quadrupole splittings and the effective field B_Q that they should induce with the actual heat capacity field B_H characterizing NSS remagnetization.

The spin temperature theory states that in a NSS isolated from the lattice, an equilibrium state characterized by the temperature Θ_N will be established within a characteristic time $T_2 \approx h/\gamma_N B_D$ [41]. On timescales larger than T_2 and shorter than T_1 , and provided that $T_2 \ll T_1$, where T_1 is the spin-lattice relaxation time, the NSS can be considered as isolated from the lattice. If NSS is prepared at temperature Θ_{Ni} under magnetic field B_i and subjected to a slowly varying magnetic field, such that $dB/dt < B_D/T_2$, then Θ_N changes, obeying the universal expression [30,41–43]

$$\frac{\Theta_N}{(B^2 + B_H^2)^{1/2}} = \frac{\Theta_{Ni}}{B_i}, \quad (5)$$

where Θ_N is related to B_N via Eq. (1).

It was assumed for many years that the heat storage in bulk semiconductor NSS is dominated by dipole-dipole interaction. Our recent measurements of the Overhauser field in the presence of the slowly varying external magnetic field overturned this assumption and pointed out the possible contribution of strain-induced quadrupole interaction; see Eq. (2) [30]. The effective field due to quadrupole interaction can be calculated as [25]

$$B_Q = \frac{4}{5} \frac{\sum_i A_i (E_{Q\perp}^2 + E_{QZ}^2)}{\sum_i A_i \gamma_{Ni}^2}. \quad (6)$$

This yields $B_Q^{\text{NMR}} = 16$ G using the quadrupole energies extracted from the NMR spectra. This value needs to be compared with B_H from Eqs. (2) and (5) that fits the remagnetization experiments.

Figure 7 shows two sets of the spin-noise spectra measured in a remagnetization experiment starting from $B_i = 0$ for two different initial nuclear-spin temperatures obtained by optical pumping during (a) 4 min and (b) 30 s. The peak in the electron spin-noise spectrum shifts from zero at $B = 0$ to ≈ 230 MHz (≈ 100 MHz) at $B_{\perp} = 100$ G in the NSS cooled during 120 (30) seconds. Longer optical cooling yields lower NSS temperature and higher Overhauser field reached in the

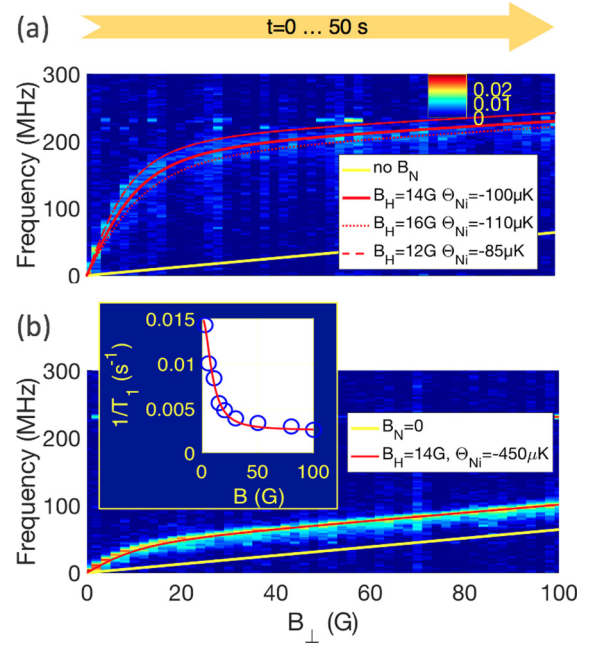


FIG. 7. Color-coded SN spectra (in signal to shot noise units) during the adiabatic demagnetization procedure preceded by preparation of nuclei including either (a) 4 min or (b) 30 s optical pumping. Red lines are fit to spin temperature model assuming $B_H = 14 \pm 2$ G and taking into account spin relaxation. Yellow line shows the external field contribution to the spin-noise frequency, F_N . Inset: the inverse nuclear-spin relaxation time as a function of the magnetic field (symbols) measured under the pumping conditions of (b). Solid line is a Lorentzian fit to the data used to calculate red lines.

former case. The contribution from the external field is identical in these two experiments. It is shown by the yellow line. One can see that the rapid growth of the frequency at small fields is followed by much slower growth at higher fields. The latter is essentially due to the external field. In the framework of the spin temperature theory, the characteristic magnetic field where the slope changes is of the order of the heat capacity field B_H . Red lines calculated using Eqs. (1), (2), (3), and (5) assuming $B_H = 14 \pm 2$ G and Θ_{Ni} as a fitting parameter are shown in Fig. 7 on top of the color-coded spin-noise spectra. The magnetic-field-dependent NSS relaxation on the timescale of the measurement (50 s) is taken into account in this calculation. The corresponding values of $1/T_1$ measured in a separate set of experiments are shown in the inset. One can see that within the experimental accuracy, which is mainly given by the unavoidable warm-up of the NSS during measurements, $B_H \approx B_Q = 14 \pm 2$ G matches quite well with the value $B_Q^{\text{NMR}} = 16$ G.

Importantly, NMR and remagnetization measurements were done at very close points on the sample surface. Indeed, it has been shown that the strain varies in the plane of GaAs substrates, epilayers, quantum wells, and microstructures [18,46–50]. A different set of NMR experiments performed at another point yielded a smaller value of $B_Q^{\text{NMR}} = 12$ G, correlated with smaller $B_Q = 9 \pm 2$ G extracted from the corresponding remagnetization experiments.

Note that the NSS relaxation enhancement at small fields has also been attributed to the presence of quadrupole effects

in the similar samples [29,51]. This so-called quadrupole relaxation is induced by fluctuating donor charges, and the resulting enhancement of the relaxation rate as compared to the relaxation rate at strong field $1/T_\infty$ is given by the same heat capacity field B_H [see Eq. (2)]:

$$\frac{1}{T_1} = \frac{1}{T_\infty} + \frac{1}{T_Q}, \quad \frac{1}{T_Q} \propto 1/(B^2 + B_H^2). \quad (7)$$

Fitting the experimental values of the NSS relaxation rate (Fig. 7, inset) to the Eq. (7) returns the value $B_Q^r = 9$ G which is slightly smaller than, but still close to, the values returned by NMR and remagnetization experiments. These results strongly support the ideas put forward in Refs. [29,30,51]. Namely, the electric field gradients in the NSS containing isotopes with the spin $I > 1/2$ lead to quadrupole effects which are detrimental to both nuclear-spin memory and adiabatic demagnetization efficiency.

VI. ESTIMATION OF GRADIENT-ELASTIC TENSOR ELEMENTS

In this section, we further analyze the quadrupole parameters determined from NMR experiments and extract relevant information on the stress intensity and orientation, as well as on the elements of the gradient-elastic tensor S_{ijkl} —an important material parameter relating electric field gradients on the atomic sites with the strain experienced by the crystal. In crystals with cubic symmetry, such as GaAs, it can be reduced to two components, S_{11} and S_{44} . The interest in this tensor has emerged recently, both in view of nondestructive characterization of the strain and in the context of exploration of coherent electron-nuclei spin dynamics in GaAs quantum dots.

The three isotope-dependent parameters that we extract from the NMR spectra are related to the three isotope-independent parameters which characterize the in-plane biaxial stress experienced by the crystal: values of the pressure applied in two orthogonal directions (p_1, p_2) and the angle ζ between the stress principal axis and [100] crystallographic axis. Their derivation is given in Appendix A 2 [52]:

$$E_{QZ}^i = -\frac{3eQ^i S_{11}^i}{4I(2I-1)C_{11}-C_{12}} \frac{p_1+p_2}{C_{11}-C_{12}}, \quad (8)$$

$$E_{Q\perp}^i \cos 2\zeta^i = \frac{3\sqrt{3}eQ^i S_{11}^i}{4I(2I-1)C_{11}-C_{12}} \frac{p_1-p_2}{C_{11}-C_{12}} \cos(2\zeta), \quad (9)$$

$$E_{Q\perp}^i \sin 2\zeta^i = \frac{\sqrt{3}eQ^i S_{44}^i}{2I(2I-1)C_{44}} \frac{p_1-p_2}{C_{44}} \sin(2\zeta). \quad (10)$$

Here, e is the absolute value of the electron charge, C_{11} , C_{12} , and C_{44} are known stiffness tensor components, and E_{Qz}^i , $E_{Q\perp}^i$, and ζ^i are the parameters of the Hamiltonian (4) determined from the fit to the NMR spectra. Their values are given in Table I.

Equations (8)–(10) are not sufficient to fully characterize five independent parameters ($p_1, p_2, \zeta, S_{11}^i, S_{44}^i$) for each isotope. However, they allow us to ascertain the ratio between the values of the gradient-elastic tensor components $S_{11}^{69\text{Ga}}/S_{11}^{75\text{As}}$ and $S_{44}^{69\text{Ga}}/S_{44}^{75\text{As}}$. Since both Ga isotopes experience the same electrostatic environment, these ratios are expected to be identical for ^{71}Ga . This appears to be the case within

our experimental precision. In the following, we denote both isotopes as Ga to simplify the notations.

The obtained values of the gradient-elastic tensor elements are summarized in Table I and compared with previous results. The component S_{11} of the gradient-elastic tensor contributes to both in- and out-of-plane quadrupole energies; see Eqs. (8) and (9). In particular, it is proportional to E_{QZ} , which dominates over in-plane quadrupole splitting $E_{Q\perp}$ in our sample. One can see that $S_{11}^{\text{Ga}}/S_{11}^{75\text{As}} = -1.1 \pm 0.1$ matches quite well with the conclusions of Refs. [16,18,19], corroborating their results.

However, for $S_{44}^{\text{Ga}}/S_{44}^{75\text{As}}$, the discrepancy between the existing values is very substantial. Our value 2.5 ± 0.4 is rather close to that of Refs. [18,19], and much smaller than the result of Ref. [20]. At this stage, we do not have any explanation for these discrepancies, but such a strong dispersion of S_{44} measured in different experiments suggests that further studies are mandatory to resolve this issue.

VII. EVALUATION OF THE BUILT-IN STRESS AND DISORDER

In order to estimate the stress parameters p_1, p_2 , and ζ , Eqs. (8)–(10) are not sufficient and we need to use the values of S_{11} measured elsewhere. We rely on recent values of Chekhovich *et al.* [16], [53]. For the point where the complete set of NMR spectra has been measured (see Fig. 5), this yields $p_1 + p_2 = 29.5$ MPa, $p_1 - p_2 = 14$ MPa, and $\zeta = 55^\circ$, bearing in mind that the relative sign of $p_1 + p_2, p_1 - p_2$, and ζ is not uniquely defined. Measurements performed at other points of the sample revealed variation of the quadrupole energies up to 30%. This is consistent with the disorder effects reported in GaAs microcavities [48–50], as well as in bulk GaAs samples [18,46]. More specifically, in our microcavity sample, due to the difference of lattice constants between GaAs and AlAs, plastic relaxation is likely to occur in the Bragg mirrors having $\approx 4 \mu\text{m}$ thickness. This relaxation is eventually accompanied by the formation of dislocations. Therefore, the lattice constant of the bottom Bragg mirror would be different from that of the GaAs cavity that we probe optically. It is not possible to give a quantitative estimation, but this difference should result in a strain in the cavity layer.

VIII. CONCLUSIONS

In this work, we develop and implement the technique that allows us to probe NMR by electron spin-noise spectroscopy. These experiments aim to quantify quadrupole effects in the NSS of n -GaAs. The NSS absorption spectra in the n -GaAs epilayer embedded in a microcavity are measured under magnetic field in the range from zero to 100 G, either parallel or perpendicular to the growth axis. The ensemble of the spectra unambiguously determines the parameters of the quadrupole Hamiltonian, and thus relevant splittings between nuclear-spin states for each of the three GaAs isotopes. These measurements are particularly relevant at zero and weak magnetic fields because the spin states splittings are dominated by quadrupole interaction rather than by the Zeeman effect, and only a few experimental methods give access to zero- and low-field NMR [18,54].

Our results establish a connection between the residual strain giving rise to quadrupole splittings, the increased heat capacity, and nuclear-spin relaxation rates at low and zero field. Indeed, from the quadrupole parameters measured by NMR, we estimate that the heat capacity field limiting NSS cooling by adiabatic demagnetization and increasing NSS spin relaxation rate is of the order of $B_Q^{\text{NMR}} = 16 \pm 2$ G. This value is close to $B_Q = 14 \pm 2$ G measured at very close point on the sample surface in a set of separate adiabatic demagnetization experiments using SNS as a detection tool. More precise measurements are complicated due to variation of up to 30% of the quadrupole energies and thus nuclear warm-up rates induced by inhomogeneity of the local strain on the scale of several millimeters across the sample surface. Nevertheless, our results strongly support the model of quadrupole-limited NSS cooling [30] and quadrupole-driven NSS warm-up [29,51].

From the quadrupole Hamiltonian, we also obtain an estimation of the gradient-elastic tensor that relates gradients of the electrostatic potential on each nuclear site with the strain tensor. Since we do not have an independent measurement of the stress present in the sample, we are limited to the determination of only relative values of the two relevant gradient-elastic tensor elements for different isotopes, S_{11} and S_{44} . It appears that $S_{11}^{\text{Ga}}/S_{11}^{75\text{As}} = -1.1 \pm 0.1$ matches quite well with the conclusions of Refs. [16,18,19], while for $S_{44}^{\text{Ga}}/S_{44}^{75\text{As}}$, where a big discrepancy exists between the values in the literature, we get $S_{44}^{\text{Ga}}/S_{44}^{75\text{As}} = 2.5 \pm 0.4$, rather close to that of Refs. [18,19], and much smaller than the result of Ref. [20]. An understanding of the discrepancies in the S_{44} values involved in the presence of an in-plane shear strain calls for further studies.

ACKNOWLEDGMENTS

The authors are grateful to R. Cherbunin and V. K. Kalevich for enlightening discussions, and acknowledge financial support from the Russian Science Foundation, Grant No. 22-42-09020, French National Research Agency, Grant No. ANR-21-CE30-0049, French Embassy in Moscow (Ostroggradski fellowship for young researchers 2020), and French RENATECH network.

APPENDIX

1. Determination of the NSS absorption from the electron spin-noise peak frequencies

An OMF $B_1 \cos(2\pi ft)$ along the z axis creates an energy flux towards NSS, $Q(f, t)$, corresponding to the energy change per one spin given by

$$Q(f, t) = \frac{\partial E_{\text{NSS}}}{\partial t} = \frac{dB_1}{dt} \sum_i A_i h \gamma_{Ni} I_{zi}, \quad (\text{A1})$$

where index i runs over all isotopes and I_{zi} is an average projection of the i th isotope spin on the OMF direction,

$$I_{zi} = \frac{B_1}{h\gamma_{Ni}} [\chi'_f \cos(2\pi ft) - \chi''_f \sin(2\pi ft)]. \quad (\text{A2})$$

Here, $\chi'_f = \chi'_{-f}$ and $\chi''_f = -\chi''_{-f}$ are the real and imaginary parts of the NSS susceptibility, respectively. Therefore, the averaged over a period energy flux towards NSS $Q(f)$ is related to its absorption $\mathcal{A}(f) = f \sum_i A_i \chi''_{fi}$ as

$$Q(f) = \pi B_1^2 \mathcal{A}(f). \quad (\text{A3})$$

On the other hand, the warm-up rate of the NSS in the presence of the OMF reads [1]

$$\frac{1}{T_w(f)} = \frac{k_B \Theta_N}{C_N} Q(f) = \pi B_1^2 \frac{k_B \Theta_N}{C_N} \mathcal{A}(f). \quad (\text{A4})$$

Here, C_N is the heat capacity of the NSS,

$$C_N = \frac{I(I+1)}{3} (B^2 + B_H^2) h^2 \sum_i A_i h \gamma_{Ni}^2, \quad (\text{A5})$$

B is an arbitrary external static field, and B_H is the heat capacity field introduced in Eq. (2). It can be rigorously determined as

$$B_H^2 = \frac{3}{I(I+1)} \frac{Sp(\hat{H}_{SS}^2)}{\sum_i A_i h \gamma_{Ni}^2}, \quad (\text{A6})$$

where \hat{H}_{SS} is the total Hamiltonian of all nuclear interactions excluding Zeeman [25]. Thus, NSS absorption at a given spin temperature is proportional to the rate of NSS warm-up induced by an OMF.

$T_w(f)$ can be extracted from the experiments described in Sec. III in the following way. Following Ref. [1] (chap. 5), we can write a detailed balance equation for the inverse nuclear-spin temperature $\beta = 1/k_B \Theta_N$ in the presence of the OMF,

$$\dot{\beta} = -\frac{1}{T_t(f)} (\beta - \beta_t), \quad (\text{A7})$$

where

$$\frac{1}{T_t(f)} = \frac{1}{T_w(f)} + \frac{1}{T_1} \quad (\text{A8})$$

is the total relaxation rate including the OMF-independent relaxation at rate T_1 , $\beta_t = \beta_0 [1 + T_w(f)/T_1]^{-1}$ is the steady-state inverse spin temperature, and β_0 is the steady-state inverse spin temperature for $B_1 = 0$.

The nuclear-spin temperature is related to the Overhauser field-induced spin-noise frequency component F_N via Eqs. (1) and (3). Therefore, from Eqs. (A7), we obtain

$$\frac{1}{T_t(f)} = \frac{1}{\Delta t_6} \ln \left[\frac{F_N(t_7)}{F_N(t_5)} \right], \quad (\text{A9})$$

where Δt_6 is the duration of stage 6 of the NMR experiment, and $F_N(t_5)$ and $F_N(t_7)$ are frequencies measured at stages 5 and 7 of the NMR experiment, respectively.

Similarly, if $B_1 = 0$, Eq. (A7) becomes

$$\dot{\beta} = -\frac{1}{T_1} (\beta - \beta_0) \quad (\text{A10})$$

and

$$\frac{1}{T_1} = \frac{1}{\Delta t_6} \ln \left[\frac{F_N^0(t_7)}{F_N^0(t_5)} \right], \quad (\text{A11})$$

where $F_N^0(t_5)$ and $F_N^0(t_7)$ are frequencies measured at stages 5 and 7 of the identical experiment but without OMF ($B_1 = 0$).

$1/T_w(f)$ is recalculated from Eqs. (A8), (A9), and (A11) for each OMF frequency. Since in the high-temperature approximation $\mathcal{A}(f) \propto \beta$, $1/T_w(f)$ does not depend on temperature and thus pertinently characterizes NSS absorption. Therefore, $1/\pi B_1^2 T_w(f)$ constitutes an NMR spectrum or, equivalently, NSS absorption spectrum. Such spectra, normalized to unity and encoded in colors, are shown in Figs. 5(a) and 5(b) for various values of static magnetic field.

2. Relation between the in-plane stress and energetic parameters of the quadrupole Hamiltonian

The second-rank tensors describing stress σ_{ij} and strain ε_{kl} are related by the fourth-rank elasticity tensor C_{ijkl} ,

$$\sigma_{ij} = \sum_{k,l} C_{ijkl} \varepsilon_{kl}. \quad (\text{A12})$$

In cubic crystals, there are only three nonzero components of the elasticity tensor:

$$\begin{aligned} C_{11} &= C_{xxxx} = C_{yyyy} = C_{zzzz}, \\ C_{12} &= C_{xxyy} = C_{yyxx} = C_{xxzz} = C_{zzxx} = C_{yyzz} = C_{zzyy}, \\ C_{44} &= C_{xyxy} = C_{yzzy} = C_{zxzx}. \end{aligned} \quad (\text{A13})$$

In a crystalline plate with the normal (z axis) parallel to the [001] axis, application of the pressure p in the structure plane at the angle ζ to the [100] axis results in the appearance of the following components of the stress tensor:

$$\begin{aligned} \sigma_{xx} &= p \cos^2 \zeta, \\ \sigma_{yy} &= p \sin^2 \zeta, \\ \sigma_{xy} &= \sigma_{yx} = p \cos \zeta \sin \zeta, \\ \sigma_{zz} &= \sigma_{zx} = \sigma_{xz} = \sigma_{zy} = \sigma_{yz} = 0. \end{aligned} \quad (\text{A14})$$

By expressing components of the stress tensor in Eq. (A14) via strain components with Eqs. (A12) and (A13), one obtains a system of linear equations for strain tensor components that yields the following solutions (see, also, problem 3 to 10th section of chap. 1 in [55]):

$$\begin{aligned} \varepsilon_{xx} &= p \frac{(C_{11} + 2C_{12}) \cos^2 \zeta - C_{12}}{(C_{11} - C_{12})(C_{11} + 2C_{12})}, \\ \varepsilon_{yy} &= p \frac{(C_{11} + 2C_{12}) \sin^2 \zeta - C_{12}}{(C_{11} - C_{12})(C_{11} + 2C_{12})}, \\ \varepsilon_{zz} &= -p \frac{C_{12}}{(C_{11} - C_{12})(C_{11} + 2C_{12})}, \end{aligned}$$

$$\begin{aligned} \varepsilon_{zx} &= \varepsilon_{xz} = \varepsilon_{zy} = \varepsilon_{yz} = 0, \\ \varepsilon_{xy} &= \varepsilon_{yx} = p \frac{\cos \zeta \sin \zeta}{C_{44}}. \end{aligned} \quad (\text{A15})$$

In the general case, the stress can be applied along two orthogonal axes in the plane. If the angle ζ defines the direction of one of the two principal axes of the stress tensor in the plane, with the principal values of this tensor being p_1 and p_2 , then, due to linearity of Eqs. (A15), we get

$$\begin{aligned} \varepsilon_{xx} &= \frac{(C_{11} + 2C_{12})(p_1 \cos^2 \zeta + p_2 \sin^2 \zeta) - C_{12}(p_1 + p_2)}{(C_{11} - C_{12})(C_{11} + 2C_{12})}, \\ \varepsilon_{yy} &= \frac{(C_{11} + 2C_{12})(p_1 \sin^2 \zeta + p_2 \cos^2 \zeta) - C_{12}(p_1 + p_2)}{(C_{11} - C_{12})(C_{11} + 2C_{12})}, \\ \varepsilon_{zz} &= -\frac{C_{12}(p_1 + p_2)}{(C_{11} - C_{12})(C_{11} + 2C_{12})}, \\ \varepsilon_{zx} &= \varepsilon_{xz} = \varepsilon_{zy} = \varepsilon_{yz} = 0, \\ \varepsilon_{xy} &= \varepsilon_{yx} = (p_1 - p_2) \frac{\cos \zeta \sin \zeta}{C_{44}}. \end{aligned} \quad (\text{A16})$$

Thus, with the knowledge of the strain components, one can find the energetic parameters of the quadrupole Hamiltonian [11]:

$$\begin{aligned} E_{QZ} &= \frac{3eQS_{11}}{2I(2I-1)} \left(\varepsilon_{zz} - \frac{\varepsilon_{xx} + \varepsilon_{yy}}{3} \right), \\ E_{QR} &= \frac{3\sqrt{3}eQS_{11}}{4I(2I-1)} (\varepsilon_{xx} - \varepsilon_{yy}), \\ E_{QI} &= \frac{\sqrt{3}eQS_{44}}{2I(2I-1)} (\varepsilon_{xy} + \varepsilon_{yx}), \end{aligned} \quad (\text{A17})$$

which amount to [cf. Eqs. (4) and (8)–(10)]

$$\begin{aligned} E_{QZ} &= \frac{3eQS_{11}}{4I(2I-1)} \frac{1}{C_{11} - C_{12}} (p_1 + p_2), \\ E_{QR} &= \frac{3\sqrt{3}eQS_{11}}{4I(2I-1)} \frac{\cos(2\zeta)}{C_{11} - C_{12}} (p_1 - p_2), \\ E_{QI} &= \frac{\sqrt{3}eQS_{44}}{2I(2I-1)} \frac{\sin(2\zeta)}{C_{44}} (p_1 - p_2). \end{aligned} \quad (\text{A18})$$

[1] *Optical Orientation*, edited by F. Meier and B. P. Zakharchenya (North Holland, Amsterdam, 1984)
[2] S. Foletti, H. Bluhm, D. Mahalu, V. Umansky, and A. Yacoby, Universal quantum control of two-electron spin quantum bits using dynamic nuclear polarization, *Nat. Phys.* **5**, 903 (2009).
[3] H. Bluhm, S. Foletti, I. Neder, M. Rudner, D. Mahalu, V. Umansky, and A. Yacoby, Dephasing time of GaAs electron-spin qubits coupled to a nuclear bath exceeding 200 μ s, *Nat. Phys.* **7**, 109 (2011).

[4] E. A. Chekhovich, M. N. Makhonin, A. I. Tartakovskii, A. Yacoby, H. Bluhm, K. C. Nowack, and L. M. K. Vandersypen, Nuclear spin effects in semiconductor quantum dots, *Nat. Phys.* **12**, 494 (2013).
[5] B. Urbaszek, X. Marie, T. Amand, O. Krebs, P. Voisin, P. Malentinsky, A. Högele, and A. Imamoglu, Nuclear spin physics in quantum dots: An optical investigation, *Rev. Mod. Phys.* **85**, 79 (2013).
[6] R. Stockill, C. Le Gall, C. Matthiesen, L. Huthmacher, E. Clarke, M. Hugues, and M. Atatüre, Quantum dot spin

- coherence governed by a strained nuclear environment, *Nat. Commun.* **7**, 12745 (2016).
- [7] D. A. Gangloff, G. Éthier-Majcher, C. Lang, E. V. Denning, J. H. Bodey, D. M. Jackson, E. Clarke, M. Hugues, C. Le Gall, and M. Atatüre, Quantum interface of an electron and a nuclear ensemble, *Science* **364**, 62 (2019).
- [8] E. V. Denning, D. A. Gangloff, M. Atatüre, J. Mørk, and C. Le Gall, Collective Quantum Memory Activated by a Driven Central Spin, *Phys. Rev. Lett.* **123**, 140502 (2019).
- [9] E. A. Chekhovich, S. F. C. da Silva, and A. Rastelli, Nuclear spin quantum register in an optically active semiconductor quantum dot, *Nat. Nanotechnol.* **15**, 999 (2020).
- [10] D. A. Gangloff, L. Zaporski, J. H. Bodey, C. Bachorz, D. M. Jackson, G. Éthier-Majcher, C. Lang, E. Clarke, M. Hugues, C. Le Gall, and M. Atatüre, Witnessing quantum correlations in a nuclear ensemble via an electron spin qubit, *Nat. Phys.* **17**, 1247 (2021).
- [11] A. Abragam, *The Principles of Nuclear Magnetism* (Clarendon Press, Oxford, 1961).
- [12] R. I. Dzhihev and V. L. Korenev, Stabilization of the Electron-Nuclear Spin Orientation in Quantum Dots by the Nuclear Quadrupole Interaction, *Phys. Rev. Lett.* **99**, 037401 (2007).
- [13] P. Maletinsky, M. Kroner, and A. Imamoglu, Breakdown of the nuclear-spin-temperature approach in quantum-dot demagnetization experiments, *Nat. Phys.* **5**, 407 (2009).
- [14] E. A. Chekhovich, K. V. Kavokin, J. Puebla, A. B. Krysa, M. Hopkinson, A. D. Andreev, A. M. Sanchez, R. Beanland, M. S. Skolnick, and A. I. Tartakovskii, Structural analysis of strained quantum dots using nuclear magnetic resonance, *Nat. Nanotechnol.* **7**, 646 (2012).
- [15] M. Kotur, D. O. Tolmachev, V. M. Litvyak, K. V. Kavokin, D. Suter, D. R. Yakovlev, and M. Bayer, Ultra-deep optical cooling of coupled nuclear spin-spin and quadrupole reservoirs in a GaAs/(Al,Ga)As quantum well, *Commun. Phys.* **4**, 193 (2021).
- [16] E. A. Chekhovich, I. M. Griffiths, M. S. Skolnick, H. Huang, S. F. Cove da Silva, X. Yuan, and A. Rastelli, Cross calibration of deformation potentials and gradient-elastic tensors of GaAs using photoluminescence and nuclear magnetic resonance spectroscopy in GaAs/AlGaAs quantum dot structures, *Phys. Rev. B* **97**, 235311 (2018).
- [17] K. Flisinski, I. Ya. Gerlovin, I. V. Ignatiev, M. Yu. Petrov, S. Yu. Verbin, D. R. Yakovlev, D. Reuter, A. D. Wieck, and M. Bayer, Optically detected magnetic resonance at the quadrupole-split nuclear states in (In,Ga)As/GaAs quantum dots, *Phys. Rev. B* **82**, 081308(R) (2010).
- [18] V. M. Litvyak, R. V. Cherbunin, V. K. Kalevich, A. I. Lihachev, A. V. Nashchekin, M. Vladimirova, and K. V. Kavokin, Warm-up spectroscopy of quadrupole-split nuclear spins in *n*-GaAs epitaxial layers, *Phys. Rev. B* **104**, 235201 (2021).
- [19] R. K. Sundfors, Experimental gradient-elastic tensors and chemical bonding in III-V semiconductors, *Phys. Rev. B* **10**, 4244 (1974).
- [20] I. M. Griffiths, H. Huang, A. Rastelli, M. S. Skolnick, and E. A. Chekhovich, Complete characterization of GaAs gradient-elastic tensors and reconstruction of internal strain in GaAs/AlGaAs quantum dots using nuclear magnetic resonance, *Phys. Rev. B* **99**, 125304 (2019).
- [21] D. Gammon, E. S. Snow, B. V. Shanabrook, D. S. Katzer, and D. Park, Fine Structure Splitting in the Optical Spectra of Single GaAs Quantum Dots, *Phys. Rev. Lett.* **76**, 3005 (1996).
- [22] M. M. Glazov, Spin noise of localized electrons: Interplay of hopping and hyperfine interaction, *Phys. Rev. B* **91**, 195301 (2015).
- [23] I. I. Ryzhov, S. V. Poltavtsev, K. V. Kavokin, M. M. Glazov, G. G. Kozlov, M. Vladimirova, D. Scalbert, S. Cronenberger, A. V. Kavokin, A. Lemaître, J. Bloch, and V. S. Zapasskii, Measurements of nuclear spin dynamics by spin-noise spectroscopy, *Appl. Phys. Lett.* **106**, 242405 (2015).
- [24] F. Berski, J. Hübner, M. Oestreich, A. Ludwig, A. D. Wieck, and M. Glazov, Interplay of Electron and Nuclear Spin Noise in *n*-Type GaAs, *Phys. Rev. Lett.* **115**, 176601 (2015).
- [25] V. K. Kalevich, K. V. Kavokin, I. Merkulov, and M. Vladimirova, Dynamic Nuclear Polarization and Nuclear Fields, in *Spin Physics in Semiconductors*, edited by M. I. Dyakonov (Springer International, Cham, 2017), pp. 387–430.
- [26] M. M. Glazov, *Electron & Nuclear Spin Dynamics in Semiconductor Nanostructures* (Oxford University Press, Oxford, 2018).
- [27] E. B. Alexandrov and V. S. Zapasskii, Magnetic resonance in the Faraday-rotation noise spectrum, *Zh. Eksp. Teor. Fiz.* **81**, 132 (1981) [*Sov. Phys. JETP* **54**, 64 (1981)].
- [28] M. Römer, J. Hübner, and M. Oestreich, Spin noise spectroscopy in semiconductors, *Rev. Sci. Instrum.* **78**, 103903 (2007).
- [29] M. Vladimirova, S. Cronenberger, D. Scalbert, M. Kotur, R. I. Dzhihev, I. I. Ryzhov, G. G. Kozlov, V. S. Zapasskii, A. Lemaître, and K. V. Kavokin, Nuclear spin relaxation in *n*-GaAs: From insulating to metallic regime, *Phys. Rev. B* **95**, 125312 (2017).
- [30] M. Vladimirova, S. Cronenberger, D. Scalbert, I. I. Ryzhov, V. S. Zapasskii, G. G. Kozlov, A. Lemaître, and K. V. Kavokin, Spin temperature concept verified by optical magnetometry of nuclear spins, *Phys. Rev. B* **97**, 041301(R) (2018).
- [31] D. Paget, G. Lampel, B. Sapoval, and V. I. Safarov, Low field electron-nuclear spin coupling in gallium arsenide under optical pumping conditions, *Phys. Rev. B* **15**, 5780 (1977).
- [32] This field was sometimes called local field despite the quadrupole contribution [33], but for the sake of clarity we prefer using the term heat capacity field.
- [33] D. Wolf, *Spin Temperature and Nuclear Spin Relaxation in Matter: Basic Principles and Applications* (Oxford University Press, Oxford, 1979).
- [34] R. Giri, S. Cronenberger, M. M. Glazov, K. V. Kavokin, A. Lemaître, J. Bloch, M. Vladimirova, and D. Scalbert, Nondestructive Measurement of Nuclear Magnetization by Off-Resonant Faraday Rotation, *Phys. Rev. Lett.* **111**, 087603 (2013).
- [35] S. Cronenberger and D. Scalbert, Quantum limited heterodyne detection of spin noise, *Rev. Sci. Instrum.* **87**, 093111 (2016).
- [36] P. Sterin, J. Wiegand, J. Hübner, and M. Oestreich, Optical amplification of spin noise spectroscopy via homodyne detection, *Phys. Rev. Appl.* **9**, 034003 (2018).
- [37] M. Y. Petrov, A. N. Kamenskii, V. S. Zapasskii, M. Bayer, and A. Greilich, Increased sensitivity of spin noise spectroscopy using homodyne detection in *n*-doped GaAs, *Phys. Rev. B* **97**, 125202 (2018).
- [38] The intended direction of the OMF was along the *z* axis. Its in-plane component is presumably due to eddy currents in the copper-based sample holder.

- [39] J. Hübner, F. Berski, R. Dabhashi, and M. Oestreich, The rise of spin noise spectroscopy in semiconductors: From acoustic to GHz frequencies, *Phys. Status Solidi B* **251**, 1824 (2014).
- [40] The dipole-dipole interaction which is known to broaden the NMR transitions, but does not lead to any shifts of their energies, is not included here [11].
- [41] A. Abragam and W. G. Proctor, Spin temperature, *Phys. Rev.* **109**, 1441 (1958).
- [42] V. K. Kalevich, V. D. Kulkov, and V. G. Fleisher, Onset of a nuclear polarization front due to optical spin orientation in a semiconductor, *JETP Lett.* **35**, 20 (1982).
- [43] V. K. Kalevich, K. V. Kavokin, Igor Merkulov, and M. R. Vladimirova, *Spin Physics in Semiconductors*, edited by M. I. Dyakonov (Springer International Publishing, Cham, 2017), pp. 387–430.
- [44] P. Pyykkö, Year-2008 nuclear quadrupole moments, *Mol. Phys.* **106**, 1965 (2008).
- [45] Y. A. Burenkov, Y. M. Burdukov, S. Y. Davidov, and S. P. Nikanorov, *Sov. Phys. Solid State* **15**, 1175 (1973).
- [46] M. Yamada, Quantitative photoelastic measurement of residual strains in undoped semi-insulating gallium arsenide, *Appl. Phys. Lett.* **47**, 365 (1985).
- [47] M. Eickhoff, B. Lenzmann, D. Suter, S. E. Hayes, and A. D. Wieck, Mapping of strain and electric fields in GaAs/Al_xGa_{1-x}As quantum-well samples by laser-assisted NMR, *Phys. Rev. B* **67**, 085308 (2003).
- [48] A. Brunetti, M. Vladimirova, S. Cronenberger, D. Scalbert, M. Nawrocki, and J. Bloch, Linear dichroism in a GaAs microcavity, *Superlattices Microstruct.* **41**, 429 (2007).
- [49] M. Abbarchi, C. Diederichs, L. Largeau, V. Ardizzone, O. Mauguin, T. Lecomte, A. Lemaître, J. Bloch, P. Roussignol, and J. Tignon, Discretized disorder in planar semiconductor microcavities: Mosaicity effect on resonant Rayleigh scattering and optical parametric oscillation, *Phys. Rev. B* **85**, 045316 (2012).
- [50] L. F. Lastras-Martínez, E. Cerda-Méndez, N. Ulloa-Castillo, R. Herrera-Jasso, L. E. Rodríguez-Tapia, O. Ruiz-Cigarrillo, R. Castro-García, K. Biermann, and P. V. Santos, Microscopic optical anisotropy of exciton-polaritons in a GaAs-based semiconductor microcavity, *Phys. Rev. B* **96**, 235306 (2017).
- [51] M. Kotur, R. I. Dzhioev, M. Vladimirova, B. Jouault, V. L. Korenev, and K. V. Kavokin, Nuclear spin warm up in bulk *n*-GaAs, *Phys. Rev. B* **94**, 081201(R) (2016).
- [52] The same formula was used in Ref. [18].
- [53] Using the values of Sundfors [19] would give approximately a factor of 1.4 smaller values of p_1 and p_2 .
- [54] J. W. Blanchard, D. Budker, and A. Trabesinger, Lower than low: Perspectives on zero- to ultralow-field nuclear magnetic resonance, *J. Magn. Reson.* **323**, 106886 (2021).
- [55] E. M. Lifshitz, A. M. Kosevich, and L. P. Pitaevskii, Fundamental equations, in *Theory of Elasticity*, 3rd ed. (Butterworth-Heinemann, Oxford, 1986), Chap. 1, pp. 1–37.

Correction: The name of a funding agency listed in the Acknowledgment section was incorrect and has been fixed.